J. Fluid Mech. (2010), *vol.* 653, *pp.* 463–487.
doi:10.1017/S0022112010000418

Influence of aspect ratio on the dynamics of a freely moving circular disk

A. R. SHENOY[1]† AND C. KLEINSTREUER[2]

[1]Department of Mathematics, University of North Carolina at Chapel Hill, Chapel Hill, NC 27599-3250, USA

[2]Department of Mechanical and Aerospace Engineering, North Carolina State University, Raleigh, NC 27695-7910, USA

(Received 23 December 2008; revised 21 January 2010; accepted 22 January 2010)

The influence of aspect ratio ($\chi =$ diameter/thickness) on the vortex shedding behaviour of fixed, and freely moving, circular disk has been investigated numerically. The aspect ratio significantly changes the structure of the vortices shed from the disk, thus altering the fluid induced forces. Disks of $\chi = 2$ and 4 were selected, and by choosing $Re = 240$ periodic behaviour was observed for both the 'fixed' and 'freely' moving disks. First, the vortex structures shed from a 'fixed' circular disk of $\chi = 2$ and 4 were computed for $Re = 240$. This was followed by a computation of their trajectories falling 'freely' under the action of gravity at $Re = 240$. For the 'fixed' disk of $\chi = 2$, periodic shedding of one-sided hairpin-shaped vortex loops was observed. The flow field had a spatial planar symmetry and the vortices were shed from the same location, resulting in an asymmetric lateral force on the disk. The Strouhal number (St), calculated using the fluctuation in the axial velocity in the far-wake, was 0.122. This vortex shedding behaviour is referred to as the 'single-sided' vortex shedding mode. For the 'fixed' disk of $\chi = 4$, periodic shedding of hairpin-shaped vortex loops was observed from the diametrically opposite location of the disk. The flow field had a spatial planar symmetry, and also a spatio-temporal one, with respect to a plane orthogonal to the spatial symmetry plane. The shed vortices induced a symmetric lateral force on the disk with a zero mean. The computed Strouhal number, was equal 0.122, same as that for $\chi = 2$. This vortex shedding behaviour is referred as the 'double-sided' vortex shedding mode. For the 'freely falling' disk of $\chi = 2$, an oscillatory motion was observed in a plane with a 83° phase lag between the lateral and angular velocity. The Strouhal number (St_b), calculated using the oscillation frequency of the 'freely' falling disk was equal to 0.116, which is comparable to the St of the fixed disk. For a 'freely falling' disk of $\chi = 4$, oscillatory motion was observed in a plane with a 21° phase lag between the lateral and angular velocity. The Strouhal number (St_b) was equal to 0.171, which differs from the St observed in the wake of the fixed disk.

1. Introduction

Circular disks moving freely under the action of gravity are known to display oscillatory motion in both angular and lateral directions (Willmarth, Hawk & Harvey 1964; Field *et al.* 1997). The oscillatory motion is an outcome of vortex shedding

† Email address for correspondence: akshenoy@yahoo.com

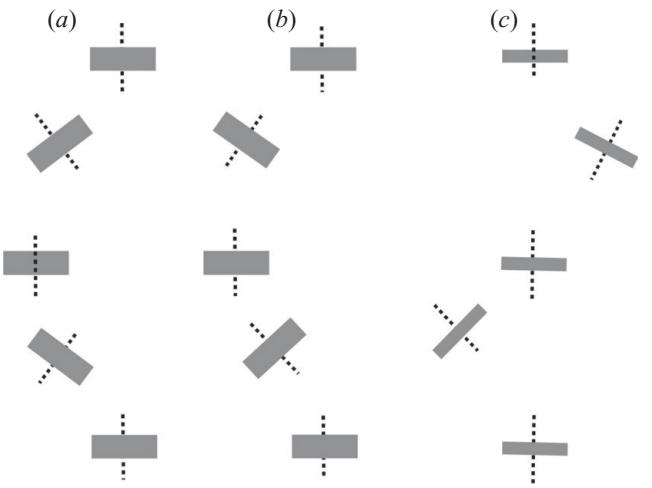

FIGURE 1. Illustration of the differences in the motion of a freely rising disk as characterized by Fernandes *et al.* (2005): (*a*) $\chi = 2 - 10$ in an inviscid fluid, $\Delta\phi = 180^\circ$, irrespective of the aspect ratio; (*b*) $\chi = 2$ in viscous fluid, $\Delta\phi \approx 0^\circ$; (*c*) $\chi = 10$ in viscous fluid, $\Delta\phi \approx 90^\circ$ ($\Delta\phi$ is the phase difference between the inclination of the disk axis and velocity with respect to the vertical direction).

behind the disk, which induces periodic forces and torques. The onset of oscillatory motion of a circular disk is governed by two non-dimensional parameters, namely the Reynolds number ($Re = \rho_f U d/\mu$), which indicates the onset of vortex shedding and the non-dimensional moment of inertia ($I^* = \pi\lambda/64\chi$, where $\chi = d/t$ is the aspect ratio and $\lambda = \rho_b/\rho_f$ is the density ratio). With increasing Reynolds number, the motion of a disk undergoes a transition from oscillatory to a continuous rotational motion, also known as tumbling or auto-rotation (Field *et al.* 1997). Although gyrational motion of circular disks about the vertical axis has been observed at very high Reynolds numbers (Stewart & List 1983), the angular motion is typically limited to an axis orthogonal to the vertical direction at medium Reynolds number. Such a gyrational motion could be due to rotation of the vortex shedding location along the circumference at higher Reynolds numbers (Berger, Scholz & Schumm 1990; Shenoy & Kleinstreuer 2008). Similar oscillatory motion has been observed for freely moving plates (Belmonte, Eisenberg & Moses 1998), spheres (Magarvey & Maclatchy 1965; Jenny, Dušek & Bouchet 2004) and cylinders (Marchildon, Clamen & Gauvin 1964).

Recent experiments by Fernandes *et al.* (2005) have indicated significant differences in the motion of freely rising disks when the aspect ratio was varied. The difference in their behaviour was quantified in terms of the phase difference ($\Delta\phi$) between the inclination of the disk axis and velocity with respect to the vertical direction. The phase difference was found to vary from -4° to 110° for the aspect ratio range $\chi =$ 1.8–15. An illustration of the influence of the aspect ratio on the motion of the disk is shown in figure 1(*a–c*). A disk in an inviscid fluid has a constant phase difference of 180°, irrespective of the aspect ratio as shown in figure 1(*a*). In figure 1(*b*), the thick disk moves with its axis nearly tangential to the trajectory ($\Delta\phi \approx 0$), whereas in figure 1(*c*) a thin disk rises with its axis nearly perpendicular to the trajectory ($\Delta\phi \approx 90^\circ$). The aspect ratio of the disk influences the structure of shed vortices which in turn influence its motion. A more recent paper (see Fernandes *et al.* 2008)

have focused on the differences in vorticity-induced forces and torques on the disk as a function of aspect ratio and their roles in affecting its motion.

Previously, Shenoy & Kleinstreuer (2008) studied the transition process of flow over a circular disk with $\chi = 10$ for $10 \leqslant Re \leqslant 300$. They observed the presence of a spatio-temporal symmetry in the wake due to alternately shed vortices, unlike the single-sided vortices observed in the wake of a sphere (Johnson & Patel 1999). The lateral forces on the disk varied symmetrically between positive and negative values, unlike for a sphere where the lateral force and torque were unidirectional. This indicates that the vortex structures are essentially different between a sphere and a thin disk and hence potentially between thick and thin disks. A recent numerical study conducted by Auguste, Fabre & Magnaudet (2010) for flow over a disk of $\chi = 3$ for a range of Reynolds numbers [150, 218] has also identified changes to the vortex structures in the wake.

The primary goal of the present study is to understand the role of aspect ratio in modifying the vortex structure behind a stationary disk and further its influence on the motion of a freely falling disk. This theoretical study is an attempt to achieve a more realistic description of non-spherical particle dynamics in dilute suspension flows. Sample applications include physiological flows such as motion of cells/platelets (Skotheim & Secomb 2007), inhaled particles and targeted drug delivery in human lung airways (Crowder *et al.* 2002; Kleinstreuer, Zhang & Donohue 2008; Wang *et al.* 2008), where non-spherical particle motion is approximated using a equivalent aerodynamic diameter, industrial applications (Yin *et al.* 2004; Ablev, Valent & Holland 2007) and Bio-MEMS (Kleinstreuer 2006). For realistic simulation of particulate flows, accurate modelling of single non-spherical particle behaviour is essential. A freely falling circular disk is considered as a prototypical non-spherical object, whose non-sphericity is quantified by the aspect ratio.

In this paper, we present the impact of the disk aspect ratio on the vortex structure in the wake of a 'fixed', and its influence on the motion of a 'freely' falling disk. The flow over stationary disks of aspect ratios $\chi = 2$ and 4 is computed at $Re = 240$, to identify the changes in vortex structures with aspect ratio. This is followed by a discussion of the motion of such disks during free fall where we observe a significant influence of the aspect ratio on the characteristics of the trajectory. The choice of $Re = 240$ ensured a periodic behaviour for both the fixed and freely moving disks of $\chi = 2$ and 4.

2. Numerical formulation

The transient three-dimensional incompressible flow fields around a stationary and freely falling circular disk of diameter d and aspect ratio ($\chi = d/t$) of 2 and 4 have been computed for $Re = 240$. The numerical solution of the incompressible Navier–Stokes equations were carried out using the finite-volume-based commercial code CFX-10.0 (ANSYS Inc., 2005). This numerical program relies on an unstructured body-fitted grid with collocated pressure and velocity nodes. The numerical algorithm is based on the SIMPLEC methodology (Van Doormaal & Raithby 1984) with Rhie–Chow interpolation scheme (Rhie & Chow 1983) to prevent the decoupling of the pressure and velocity fields, typically observed on collocated grids. A second-order implicit backward-Euler scheme for time stepping was used, while the advection terms were evaluated using a high-resolution scheme (Barth & Jespersen 1989). A hexahedral mesh with an O-grid topology was generated using the commercial grid generation software ICEM-CFD (ANSYS Inc., 2007). A refined mesh was implemented close

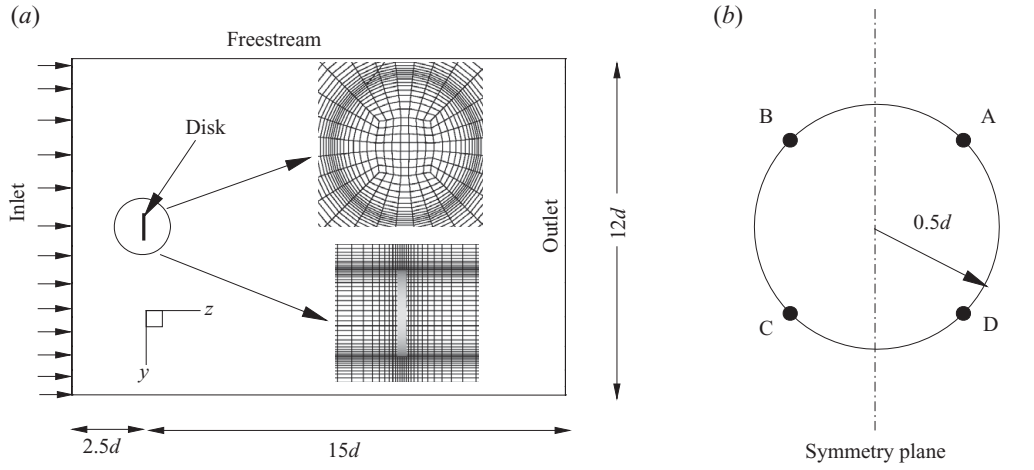

FIGURE 2. Stationary disk: (*a*) Computational domain and grid structure for flow over a stationary disk; (*b*) axial velocity sampling locations (A, B, C and D) at $z = 5d$ at a radial distance of $0.5d$ and a azimuthal spacing of 90°.

to the surface of the disk in both axial and radial directions to accurately capture steep gradients. For computing the motion of the freely moving disk, an arbitrary Lagrangian–Eulerian (ALE) formulation was used. The six degrees of freedom of the disk motion was coupled to the fluid solver, using a pseudo-implicit algorithm.

Identification of the vortical regions was performed using the λ_2-criterion proposed by Jeong & Hussain (1995), namely

$$\lambda_2(\boldsymbol{S}^2 + \boldsymbol{\omega}^2) < 0, \tag{2.1}$$

where λ_2 is the intermediate eigenvalue of the symmetric tensor $\boldsymbol{S}^2 + \boldsymbol{\omega}^2$, while $\boldsymbol{S}$ and $\boldsymbol{\omega}$ are the rate of strain and vorticity tensors, respectively. Although numerous techniques exist for identifying the vortex regions, including a frame-independent method proposed by Haller (2005), we have decided to use the λ_2-criterion for comparison with existing numerical results.

2.1. *Stationary disk*

A cylindrical computational domain with a cross-section of diameter $D_c = 12d$ was situated along the z direction (see figure 2) with the centre of the disk located on the z-axis and its upstream surface in the xy plane. The domain extended $z_d = 15d$ downstream and $z_u = 2.5d$ upstream of the disk. The domain was discretized into 59 556 elements with 61 836 nodes. The non-dimensional forms of the Navier–Stokes equations (2.2) were solved with the boundary conditions given in (2.4):

$$\frac{\partial \boldsymbol{V}}{\partial t} + \boldsymbol{V} \cdot \nabla \boldsymbol{V} = -\nabla p + \frac{1}{Re} \nabla^2 \boldsymbol{V}, \tag{2.2}$$

$$\nabla \cdot \boldsymbol{V} = 0, \tag{2.3}$$

$$\boldsymbol{V}(x, y, z_u, t) = (0, 0, 1); \quad \boldsymbol{V}(x, y, z, t)|_{\partial\sigma} = 0; \quad p(x, y, z_d, t) = 0, \tag{2.4}$$

where $\partial\sigma$ and $\partial\Sigma$ represent the surface of the disk and free stream, respectively. A fixed time step (Δt) which yielded approximately 100 points in one period of the dominant frequency was used along with the stability criterion of $CFL < 1$. The time history of the axial velocity was recorded at $z = 5d$ from the rear surface of the disk. At each axial location, the velocity was sampled at four points (A, B, C, D)

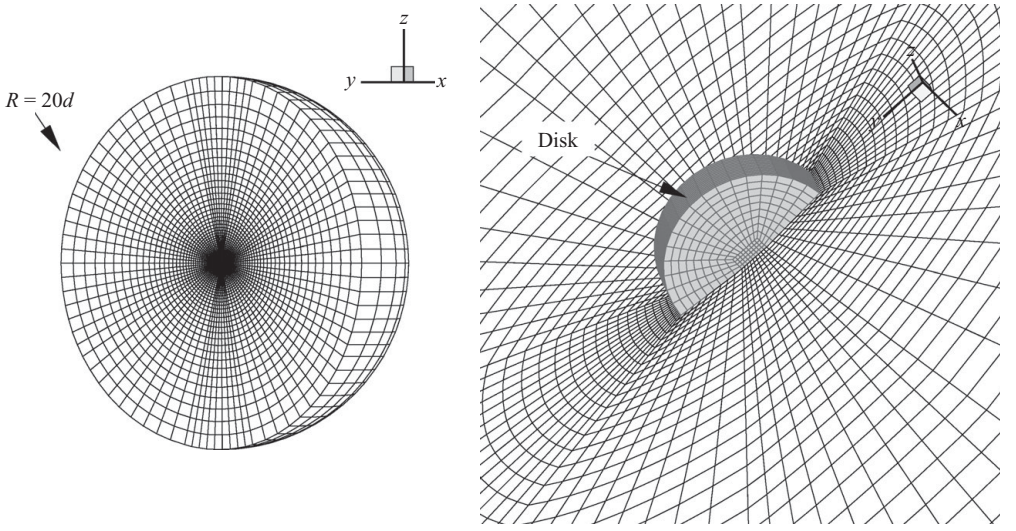

FIGURE 3. Falling disk: (*a*) computational domain and grid structure for a freely moving disk falling vertically along the negative *z-axis*; (*b*) grid structure in the neighbourhood of the disk.

at a radial distance of $5d$ and azimuthal spacing of 90° (see figure 2*b*). The effects of computational domain size and grid spacing on the results have been previously evaluated by Shenoy & Kleinstreuer (2008) and were found to be negligible. The drag coefficient (C_d) in the axial direction was computed for the Reynolds number range of 10–100 and compared with experimental results by Ross & Willmarth (1971) showing a good match. Further comparison with computational results of the vortex shedding frequency (Fernandes *et al.* 2007) has been included to validate our computational results (see § 3).

2.2. *Moving disk*

A moving grid formulation was employed for computing the motion of the freely falling disk. The grid was fixed to the disk surface and the computational domain moved along with the disk. The computational domain consisted of a spherical volume of radius $R = 20d$ (see figure 3*a*) that enclosed a circular disk located at the origin, with its axis oriented along the z direction. All the simulations were performed using a grid of 253 346 elements with 257 760 nodes. The motion of the body was computed in the moving non-inertial xyz-coordinate system fixed to the centroid of the disk and oriented along its principal axis, as shown in figure 4. The fluid computations were performed in the fixed coordinate system, namely XYZ. The body parameters in the XYZ-coordinate system are identified by tilded variables ($\tilde{\boldsymbol{U}}$, $\tilde{\boldsymbol{\Omega}}$, $\tilde{\boldsymbol{F}}$, $\tilde{\boldsymbol{T}}$).

To compute the fluid motion in a moving grid configuration, an integral formulation of the governing equations (Demirdžić & Peric 1990) was used:

$$\frac{\mathrm{d}}{\mathrm{d}t}\iiint_{\mathscr{V}} \rho \,\mathrm{d}\mathscr{V} + \iint_{\partial\mathscr{V}} \rho(\boldsymbol{V}-\boldsymbol{W})\cdot\mathrm{d}\boldsymbol{S} = 0, \tag{2.5}$$

$$\frac{\mathrm{d}}{\mathrm{d}t}\iiint_{\mathscr{V}} \rho\,\boldsymbol{V}\,\mathrm{d}\mathscr{V} + \iint_{\partial\mathscr{V}} [\rho(\boldsymbol{V}-\boldsymbol{W})\boldsymbol{V} - \boldsymbol{\Pi}]\cdot\mathrm{d}\boldsymbol{S} = 0. \tag{2.6}$$

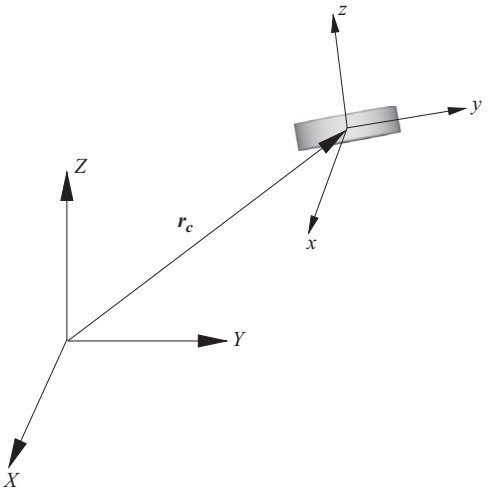

FIGURE 4. Coordinate systems used for computing body motion. XYZ : fixed coordinate system used for computing fluid motion; xyz : moving coordinate system fixed to the disk used for computing body motion.

The control volume $\mathscr{V}$ is bounded by a surface $\partial\mathscr{V}$ which moves with the velocity $\boldsymbol{W}$. The stress tensor $\boldsymbol{\Pi}$ for incompressible Newtonian fluid is given as

$$\boldsymbol{\Pi} = -p\boldsymbol{I} + \mu(\nabla\boldsymbol{V} + \nabla\boldsymbol{V}^T). \tag{2.7}$$

In addition to these equations, the space conservation law needs to be satisfied to prevent artificial mass sources (Demirdžić & Peric 1988):

$$\frac{\mathrm{d}}{\mathrm{d}t}\iiint_{\mathscr{V}} \mathrm{d}\mathscr{V} - \iint_{\partial\mathscr{V}} \boldsymbol{W}\cdot\mathrm{d}\boldsymbol{S} = 0. \tag{2.8}$$

The following boundary conditions were applied to the surface of the disk ($\partial\sigma$) and the far field ($\partial\Sigma$):

$$(\boldsymbol{V} - \boldsymbol{W})|_{\partial\sigma} = 0, \quad p(\partial\Sigma, t) = 0. \tag{2.9}$$

The computational domain surrounding the disk moves with the disk and has a grid velocity given by

$$\boldsymbol{W}(\boldsymbol{r}, \boldsymbol{t}) = \tilde{\boldsymbol{U}}(t) + \tilde{\boldsymbol{\Omega}}(t) \times (\boldsymbol{r} - \boldsymbol{r_c}), \tag{2.10}$$

where $\tilde{\boldsymbol{U}}$ and $\tilde{\boldsymbol{\Omega}}$, are the translational and angular velocity of the body whose centre of mass is located at $\boldsymbol{r_c}$ with respect to the XYZ-coordinate system. It can be easily seen that this grid motion satisfies the geometric conservation law (2.8). The force and torque acting on the disk due the fluid are computed as

$$\tilde{\boldsymbol{F}} = \int\int_{\partial\sigma} \boldsymbol{\Pi}\cdot\mathrm{d}\boldsymbol{S}, \; \tilde{\boldsymbol{T}} = \int\int_{\partial\sigma} (\boldsymbol{r} - r_c) \times \boldsymbol{\Pi}\cdot\mathrm{d}\boldsymbol{S}. \tag{2.11}$$

The above equations compute the flow field for a prescribed motion of the grid points which move with the disk. In the present case, the grid points do not move relative to each other but the entire computational domain is rotated and translated along with the disk according to the relationship (2.10). In this paper, we used a pseudo-implicit scheme in which the inviscid contributions are treated implicitly but the viscous contributions are treated explicitly. A generalized Kirchhoff–Kelvin equation

was used to describe the body motion (Mougin & Magnaudet 2002):

$$(m\boldsymbol{I} + \boldsymbol{A})\frac{\mathrm{d}\boldsymbol{U}}{\mathrm{d}t} + \boldsymbol{\Omega} \times (m\boldsymbol{U}) = \boldsymbol{F} + (m - m_f)\boldsymbol{g}, \tag{2.12}$$

$$(\boldsymbol{J} + \boldsymbol{D})\frac{\mathrm{d}\boldsymbol{\Omega}}{\mathrm{d}t} + \boldsymbol{\Omega} \times (\boldsymbol{J}\boldsymbol{\Omega}) = \Gamma, \tag{2.13}$$

where $\boldsymbol{A}$, $\boldsymbol{D}$ are the added mass tensors for translational and rotational motion, respectively; $\boldsymbol{J}$ is the moment of inertia tensor; $m_f = \rho_f \pi d^3/4\chi$ is the mass of the displaced fluid; and $\boldsymbol{g}$, $\boldsymbol{U}$ and $\boldsymbol{\Omega}$ are the linear velocity, angular velocity and gravitational vector, respectively, in the xyz-coordinate system. These tensors are diagonal if the coordinate system is aligned with the principal axes of the body and independent of the body orientation, as the xyz-coordinate system is fixed to the body and hence needs to be computed only once (see Appendix A for details). The cross-product terms in (2.12) and (2.13) are due to the non-inertial frame of reference, namely xyz.

The orientation of the body-fixed coordinate system, relative to the global coordinate system was expressed using the x-convention of the Euler angles (ϕ, θ, ψ), as described in Goldstein, Poole & Safko (2002). Due to the singularity in the equation governing the rate of change in Euler angles, the Euler parameters $\Theta = (\varepsilon_1, \varepsilon_2, \varepsilon_3, \eta)^T$ were used for tracking the body orientation, replacing the Euler angles. The Euler angles were then back calculated from the Euler parameters. The equations governing the change in the Euler parameters is given by

$$\frac{\mathrm{d}\Theta}{\mathrm{d}t} = \boldsymbol{E}\,\boldsymbol{\Omega}, \tag{2.14}$$

where $\boldsymbol{E}$ is a function of Θ (see Appendix B for details). Since the fluid computations were performed in the XYZ-coordinate system, the fluid forces on the disk need to be transformed to the xyz-coordinate system using the rotational matrix $\boldsymbol{R}$, which is a function of Θ:

$$\left[\boldsymbol{F},\, \boldsymbol{T},\, \boldsymbol{g}\right]^T = \boldsymbol{R}\,\left[\tilde{\boldsymbol{F}},\, \tilde{\boldsymbol{T}},\, \tilde{\boldsymbol{g}}\right]^T, \tag{2.15}$$

$$\left[\tilde{\boldsymbol{U}},\, \tilde{\boldsymbol{\Omega}}\right] = \boldsymbol{R}^T\,\left[\boldsymbol{U},\, \boldsymbol{\Omega}\right]^T. \tag{2.16}$$

The velocity of the body $(\boldsymbol{U}, \boldsymbol{\Omega})$ in the xyz-coordinate system was determined by solving (2.12). The grid velocity $(\boldsymbol{W})$ was then obtained by transforming the body velocity into the XYZ-coordinate system using (2.10) and (2.16). The above system of equations produced stable results for $CFL < 1$. The equations for the body dynamics were solved using a Runge–Kutta solver (RK45) (Press *et al.* 1992).

The oscillatory motion of the disk did not significantly influence the vertical velocity, a fluctuation of $\pm 1.2\,\%$ was observed. The Reynolds number was then calculated using the average vertical velocity $(\bar{U}_\infty)$. The computed average terminal was compared with theoretical velocity assuming a drag coefficient $C_{d,\infty} = 1.2$ for all aspect ratios (Ross & Willmarth 1971). The computed results for the terminal velocity in table 1 show good comparison with theoretical calculations. To validate the numerical model, sedimentation of a sphere starting from rest was computed for two different Reynolds numbers, namely $Re = 41$ and 280. The temporal evolution of the sphere velocity (U) was compared with experimental results obtained by Mordant & Pinton (2000) for a freely falling sphere over a wide range of Reynolds numbers (40–70 000). For that Reynolds number range, the following similarity relationship

χ	$\nu \times 10^4$	$U_\infty = \sqrt{\frac{2(\lambda-1)gd}{\chi\, C_{d,\infty}}}$ (Theoretical)	$\bar{U}_\infty$ (Numerical)
2	11.91	0.286	0.290
4	8.42	0.202	0.196
5	7.53	0.181	0.178
6	6.87	0.165	0.160
8	5.95	0.143	0.150
10	5.33	0.128	0.132

TABLE 1. Comparison of theoretically estimated velocity values with numerical results for $Re = 240$ using $C_{d,\infty} = 1.2$, $d = 1$, $\rho_f = 1$, $\rho_b = 1.01$, $g = 9.8$.

was observed:

$$u^*(t^*) = \frac{U}{U_\infty} = 1 - \mathrm{e}^{-t^*}, \tag{2.17}$$

where U_∞ is the terminal velocity, $t^* = 3t/t_{95}$, and t_{95} is the time at which $U = 0.95\,U_\infty$. A comparison of the experimental result with present computations is shown in figure 5(*a*), which indicates a good match for both $Re = 41$ and 280.

Temporal evolution of the terminal velocity during the sedimentation of circular disks of aspect ratios 1, 2, 6 and 10 was computed at $Re = 41$ (see figure 5*b*). The temporal evolution of the different disks do not fall on a single curve, potentially due to differences in C_d at the lower Reynolds numbers where frictional forces play a crucial role as well as the boundary layer development (Basset history term). The sedimentation velocity history for $\chi = 10$ and $Re = 41$ was used as a test case to determine the effects of domain size and grid resolution (see figure 5*c*). Computations were performed using a larger computational domain of size $R = 30d$ with the same grid spacing as used in the previous computations. Furthermore, grid interdependence was verified by using a finer mesh (543 366 elements and 535 392 nodes).

Next we compare the computed phase difference ($\Delta\phi$) between the inclination of the disk axis and velocity with respect to the vertical direction with experimental results (Fernandes *et al.* 2005) at $Re = 240$ (see figure 6). We observe a good match for $\chi = 6$, 8 and 10, with a discrepancy for $\chi = 2$ and 4. The overall trend of an increasing phase difference with aspect ratio has been accurately predicted. A comparison of the oscillation frequencies of freely rising disks (Fernandes *et al.* 2007), namely Strouhal number $St = 0.107$ for $\chi = 2$ and $St = 0.261$ for $\chi = 10$, confirm our computational results of $St = 0.116$ for $\chi = 2$ and $St = 0.242$ for $\chi = 10$, respectively. The above results indicate that the numerical scheme and computational parameters have been sufficiently validated against available experimental data.

3. Results

Numerical computations of flow over a 'fixed' disk of $\chi = 2$ and 4 were performed at $Re = 240$. Periodic vortex shedding was observed for both aspect ratios but with significantly different vortex structures, which influenced the forces acting on the disks. Two different vortex shedding modes were observed, namely: (*a*) 'single-sided' vortex shedding, for $\chi = 2$, (*b*) 'double-sided' vortex shedding, for $\chi = 4$. Next, we computed the motion of the above mentioned disks, falling 'freely' under the action of gravity

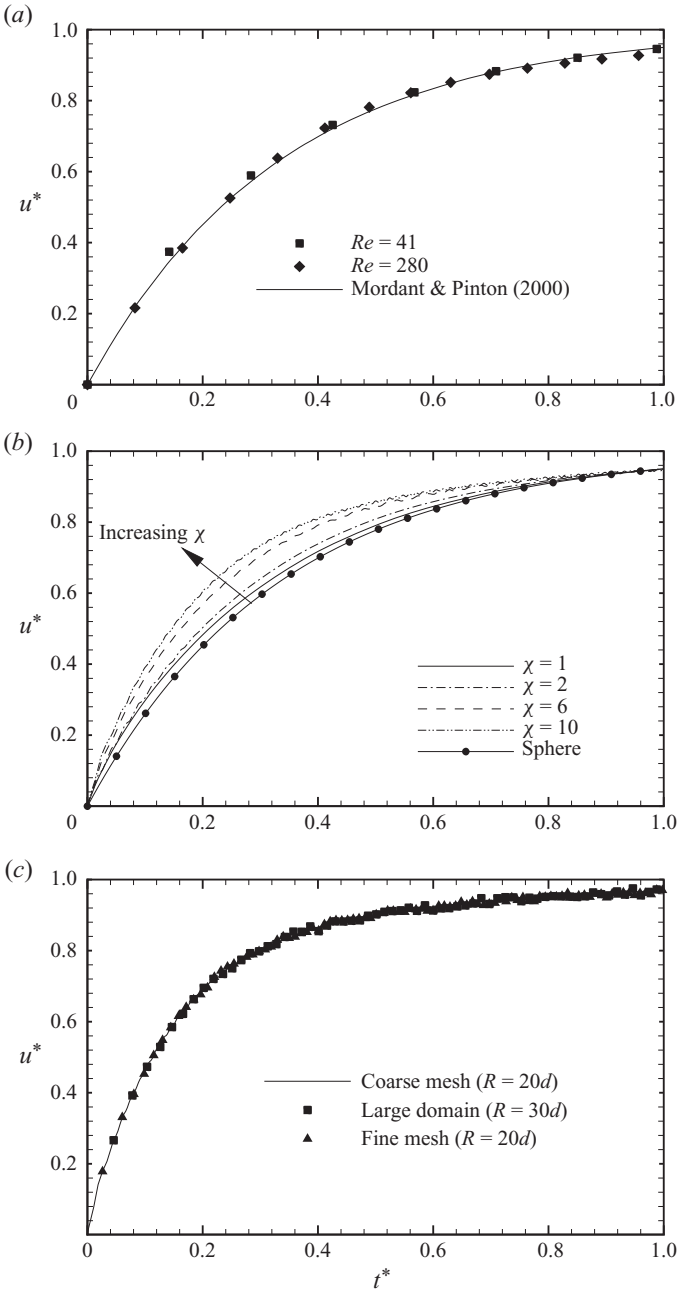

FIGURE 5. Validation of the computational model by a comparison of the computed temporal evolution of the vertical velocity: (*a*) freely falling sphere at $Re = 41$ and 280, compared against the experimental results obtained by Mordant & Pinton (2000); (*b*) freely falling disk, with different aspect ratios, at $Re = 41$ showing the influence of the aspect ratio; (*c*) freely falling disk at $Re = 41$ and $\chi = 10$ computed for both 'coarse' and 'fine' mesh with a domain size of $R = 20d$, and a larger domain of size $R = 30d$.

χ	Vortex structure	Symmetry	St	Lateral force
2	Single-sided	Spatial plane	0.122	Asymmetric
4	Double-sided	Spatial plane and a spatio-temporal	0.122	Symmetric

TABLE 2. Summary of the computed vortex shedding behaviour behind a fixed circular disk at $Re = 240$, where the Strouhal number St is calculated using the axial velocity fluctuations.

χ	Lateral amplitude	Angular amplitude	$\Delta\Phi$	St_b
2	$0.232d$	26.82°	83°	0.116
4	$0.159d$	25.71°	21°	0.171

TABLE 3. Summary of the motion of a freely moving circular disk at $Re = 240$, where d is the diameter of the disk, $\Delta\Phi$ is the phase difference between lateral and angular velocity and St_b is the Strouhal number calculated using the body oscillations.

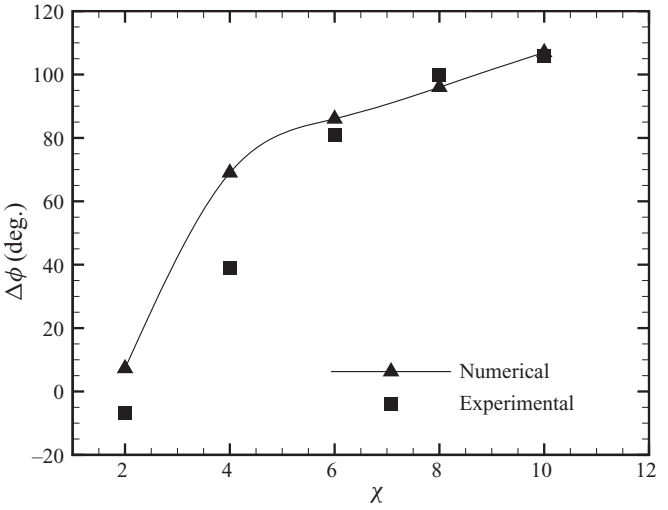

FIGURE 6. Comparison of the computed phase difference ($\Delta\phi$) with experimental data (Fernandes *et al.* 2005).

at $Re = 240$ (based on the mean vertical velocity). Periodic oscillatory motion was observed for both the disks but their trajectories differed in terms of the phase relationship between the lateral and angular oscillations. The disk of $\chi = 2$ oscillated with a Strouhal number (St_b) nearly equal to that observed for the fixed disk due to vortex shedding. In contrast, the disk $\chi = 4$ oscillated at a higher frequency than the vortex shedding observed behind the fixed disk. A summary of the observed results is provided in table 2 for the fixed disk and table 3 for the freely moving disk.

3.1. *Fixed disk*

In this section, we describe the vortex shedding phenomena observed behind a fixed disk of $\chi = 2$ and 4 at $Re = 240$. Periodic shedding of hairpin-shaped vortex loops was observed in the wake of both the disks at a Strouhal number ($St = fd/U$) of 0.122. For $\chi = 2$, the vortex loops were oriented along the same direction hence refereed to as 'single-sided' by Perry, Lim & Chong (1980) and as the 'zig-zig' mode by Auguste *et al.* (2010). Similar vortex structure have been observed in the wake of a sphere

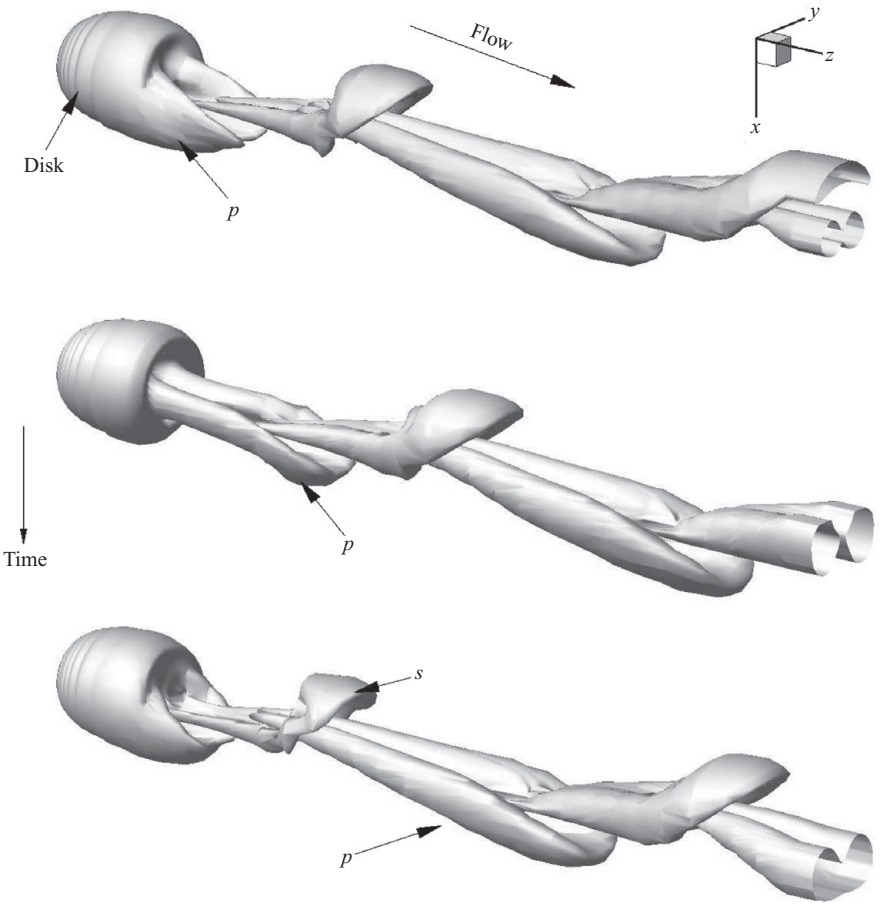

FIGURE 7. Temporal evolution of vortex structures visualized using the λ_2-criterion for the 'single-sided' vortex shedding mode, in the wake of a fixed disk of $\chi = 2$ at $Re = 240$, with the free-stream oriented along the positive z direction. The vortex structure shed from the disk is marked p and the induced vortex structure is marked s.

at moderate Reynolds numbers (Achenbach 1974). The vortex structures observed in the wake were visualized using the λ_2-criterion and are shown in figure 7 for a single vortex shedding period. For more detailed visualizations, animations of the vortex shedding process have been included in the on-line supplementary material (Movie 1, available at journals.cambridge.org/flm).

For $\chi = 4$, the vortex loops were shed alternately from diametrically opposite location of the disk; a three-dimensional version of the vortex street observed behind a $2d$ cylinder, hence refereed to as 'double-sided' by Perry *et al.* (1980) and as the 'zig-zag' mode by Auguste *et al.* (2010). Experimental evidence of double-sided vortices in a wake have been previously reported by Perry *et al.* (1980) and Brücker (2001). The vortex structures observed in the wake were visualized using the λ_2-criterion and are shown in figure 8 for a single vortex shedding period. For more detailed visualizations, animations of the vortex shedding process have been included in the on-line supplementary material (Movie 2).

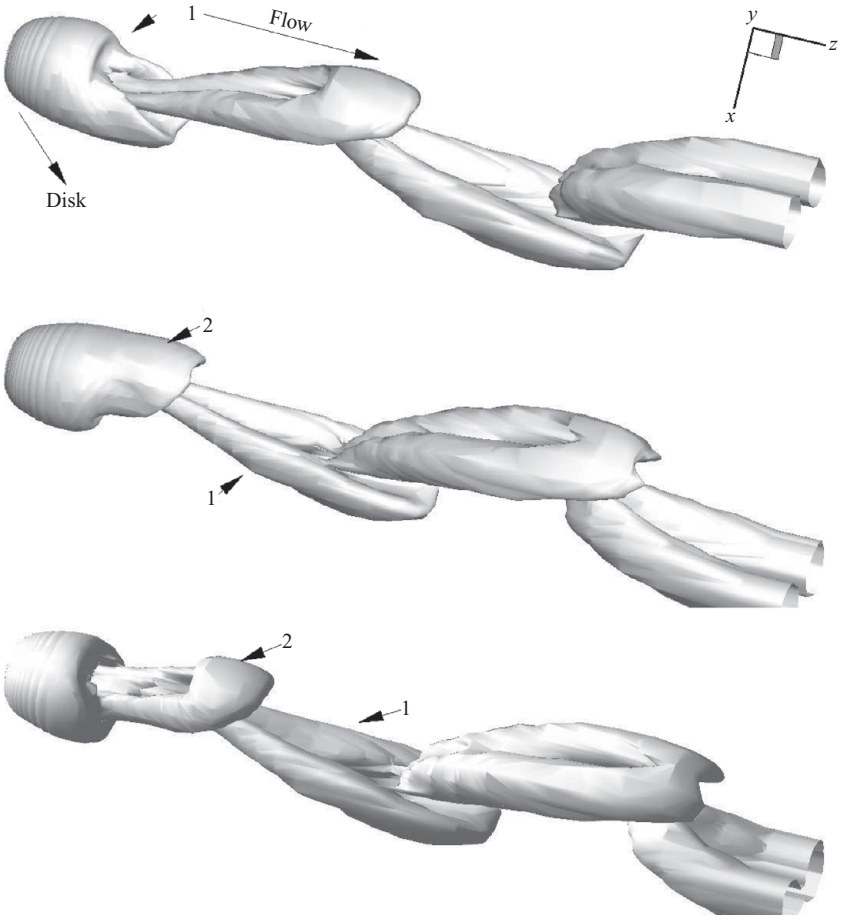

FIGURE 8. Temporal evolution of vortex structures visualized using the λ_2-criterion for the 'double-sided' vortex shedding mode, in the wake of a fixed disk of $\chi = 4$ at $Re = 240$, with the free-stream oriented along the positive z direction. The vortex structure shed from the disk is marked 1 and 2.

3.1.1. *Single-sided vortex shedding*

In this section, we describe the single-sided vortex shedding observed behind the disk of $\chi = 2$ (see figure 7). This mode is characterized by one-sided vortex loops shed from the wake (labelled p in figure 7) from a fixed azimuthal location. Also observed in figure 7 is an induced vortex (labelled s) formed near the leg of the separating vortex (p). This induced vortex has an opposite sign as the shed vortex and is generated due to the interaction of the near wake flow to separating vortex. This wake structure bears strong similarity to that observed behind a sphere by Johnson & Patel (1999). Shedding of the single-sided vortex (p) induces asymmetric lateral force and torque on the disk. The vortex structure (s) is not shed from the wake and hence does not induce any force/torque on the body. Further, a symmetry plane normal to the xy plane and passing through the z-axis was observed. The orientation of this plane to the x-axis was a function of the bias induced by the numerical approximation. The symmetry plane is shown in figure 9, where the axial vorticity contours are projected

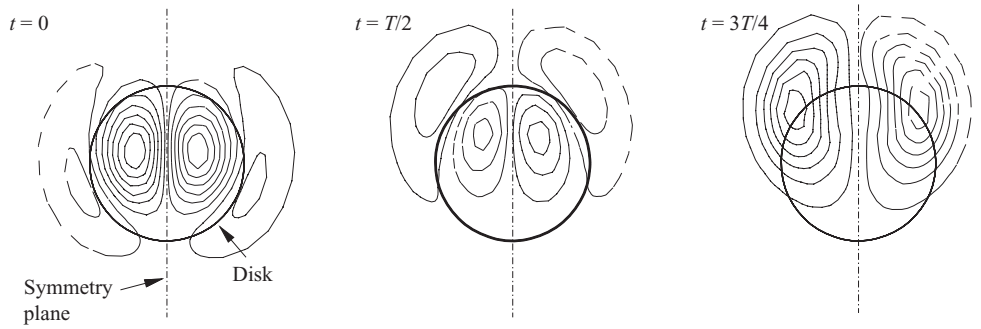

FIGURE 9. Axial vorticity (ω_z) contours projected on the xy plane at $z = 5d$, for three different time intervals of the period T, indicating the presence of a symmetry plane during 'single-sided' vortex shedding for $\chi = 2$ at $Re = 240$.

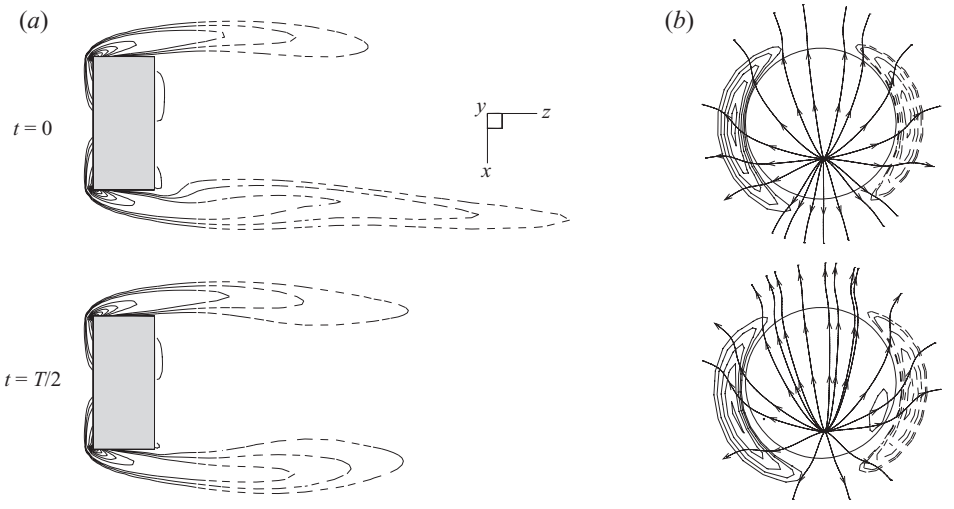

FIGURE 10. Flow structures in the near wake region of a fixed disk of $\chi = 2$ at $Re = 240$ for two temporal locations separated by half the period, namely T: (a) azimuthal vorticity contours projected onto the symmetry plane; (b) limiting streamlines (shown with arrows) and axial vorticity contours projected on the xy plane near the disk surface, where solid and dashed contour lines indicate positive and negative values, respectively.

on a xy plane at $z = 5d$ for three different temporal locations. Presence of a symmetry plane implies that there are no lateral forces normal to the symmetry plane.

To further understand the nature of the vortex structures, the azimuthal vorticity (ω_θ) contours projected onto the symmetry plane are shown in figure 10(a) for two different time intervals separated by half the period of the vortex shedding period (see online supplementary material Movie 3). The vorticity contours clearly indicate the asymmetric vortex shedding observed for $\chi = 2$, where vorticity is shed only from the bottom part of the wake. The limiting streamlines near the rear surface of the disk, along with the axial vorticity (ω_z) contours, are shown in figure 10(b). The axial vorticity contours indicate the presence of a vorticity dipole for 'single-sided' mode. The limiting streamlines near the disk surface form a stationary node on the rear surface of the disk, which remains stationary throughout the vortex shedding cycle, similar to that observed for a sphere (Johnson & Patel 1999).

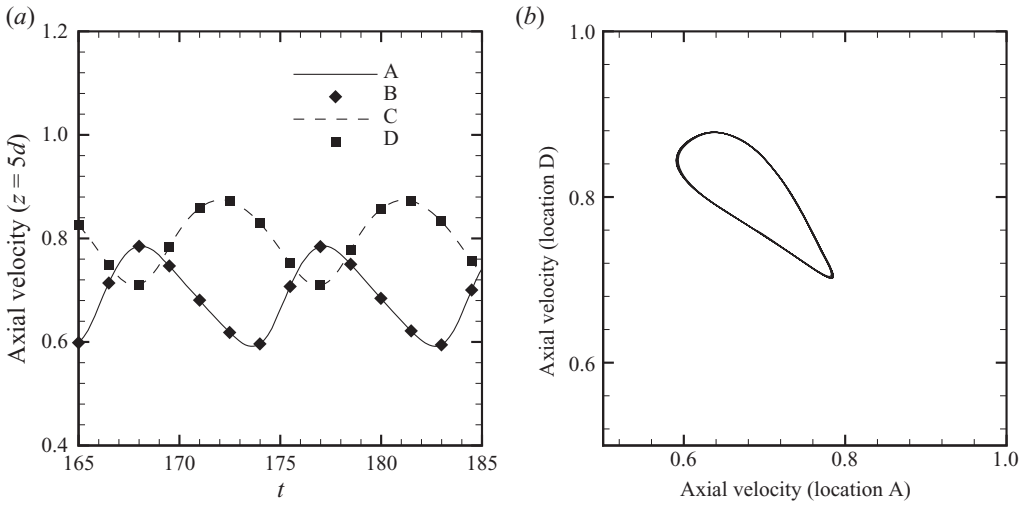

FIGURE 11. Influence of the 'single-sided' vortex shedding mode on the axial velocity variation in the wake at $z = 5d$ for $\chi = 2$ at $Re = 240$: (a) temporal variation of axial velocity at angular location of A, B, C and D (see figure 2b); (b) Lissajous pattern of axial velocity at locations A and D.

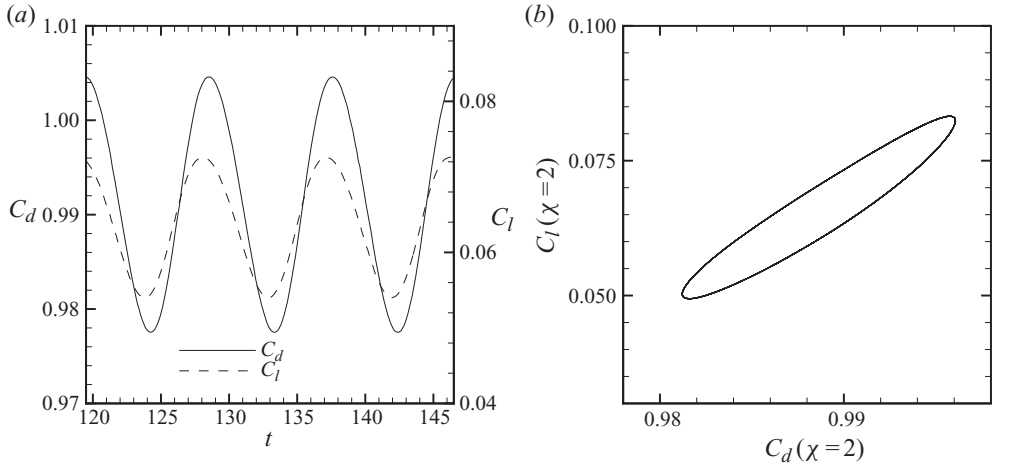

FIGURE 12. Influence of the 'single-sided' vortex shedding mode on the drag (C_d) and lift coefficient (C_l) for $\chi = 2$ at $Re = 240$: (a) temporal variation of C_d and C_l; (b) Lissajous plot of C_d and C_l.

Next we look in figure 11(a) the temporal variation of axial velocity sampled at the location $z = 5d$ (see figure 2b). The velocity in the wake fluctuated at $St = 0.122$. A comparison of the axial velocities at locations A, B, C and D, shown in figure 11(a), indicates the presence of a symmetry plane, as the velocity at location A matches that at B; similarly, there is a correlation between axial velocity at locations C and D. Furthermore, a phase difference of 180° was observed between the velocity fluctuations at locations A and D. A Lissajous plot of the axial velocity fluctuation is shown in figure 11(b), where we observe that for $\chi = 2$ there is a single loop. In the figure 12(a), periodic variation of the drag (C_d), and lift coefficient (C_l), which was computed using the lateral force acting along the symmetry plane, is shown. The drag,

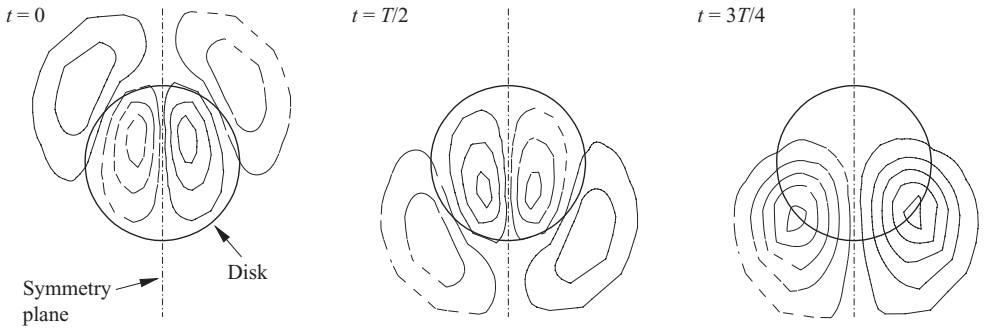

FIGURE 13. Axial vorticity (ω_z) contours projected on the xy plane at $z = 5d$ for three different time intervals of the period T, indicating the presence of a symmetry plane during single-sided vortex shedding for $\chi = 4$ at $Re = 240$.

and lift coefficient, were found to vary at the same frequency as the axial velocity fluctuation for the 'single-sided' mode with C_l having a phase lead of $\approx 10^\circ$. In fact, C_l did not change sign, remaining positive in this case, through-out the period. A Lissajous plot of C_d and C_l, shown in figure 12(b) also indicates a single loop. We also performed simulations for a disk with $\chi = 1$ at $Re = 400$ as no vortex shedding occurred at $Re = 240$ and also observed the 'single-sided' mode. The 'single-sided' vortex shedding leads to asymmetric forces and torque acting on the disk.

3.1.2. *Double-sided vortex shedding*

In this section, we describe the double-sided vortex shedding observed behind $\chi = 4$ (figure 8). In contrast to that observed for $\chi = 2$, the vortex structures shown in figure 8 for $\chi = 4$ consist of two vortices, namely 1 and 2 of equal strength but opposite sign and they shed from diametrically opposite locations of the disk. This difference in vortex shedding indicates that the wake structure is a function of the aspect ratio, along with the previously known influence of the Reynolds number (Shenoy & Kleinstreuer 2008; Auguste *et al.* 2010). A spatial symmetry plane was observed, similar to that for $\chi = 2$, along with a spatio-temporal plane orthogonal to the spatial symmetry plane. The shedding of symmetric oppositely oriented vortices is reminiscent of the flow structures behind a two-dimensional cylinder (Barkley & Henderson 1996). Due to the symmetric vortex shedding we can expect the lateral forces and torques to vary symmetrically between positive and negative values, i.e. with a zero mean. The symmetry plane is shown in figure 13, where the axial vorticity contours are projected on a xy plane at $z = 5d$ for three different temporal locations. Figure 13 also illustrates the observed spatio-temporal symmetry.

To further understand the nature of the vortex structures, the azimuthal vorticity (ω_θ) contours projected onto the symmetry plane are shown in figure 14(a) at two different time intervals separated by half the period of the velocity fluctuation, namely T. The vorticity contours indicate a symmetric shedding from the top and bottom part of the wake (see online supplementary material Movie 4). The limiting streamlines near the rear surface of the disk, along with the axial vorticity (ω_z) contours are also shown in figure 14(b). The axial vorticity contours indicate the presence of a vorticity quadrupole. The limiting streamlines form a stretched node, and it displays lateral motion during the vortex shedding cycle.

In figure 15(a), we look at the temporal variation axial velocity sampled at the axial location of $z = 5d$ (see figure 2b). The velocity in the wake fluctuated with

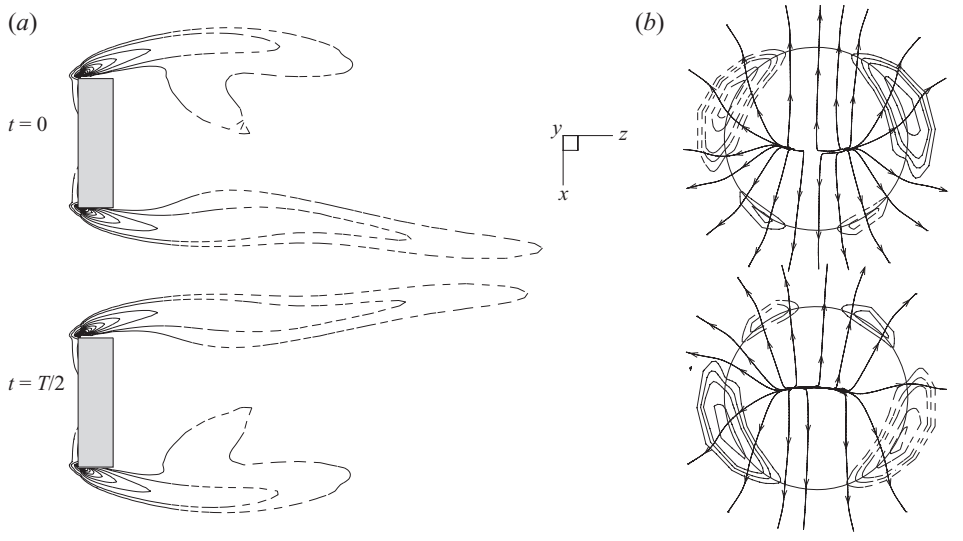

FIGURE 14. Flow structures in the near wake region of a fixed disk of $\chi = 4$ at $Re = 240$ for two temporal locations separated by half the period, namely T: (a) azimuthal vorticity contours projected onto the symmetry plane; (b) limiting streamlines (shown with arrows) and axial vorticity contours projected on the xy plane near the disk surface, where solid and dashed contour lines indicate positive and negative values, respectively.

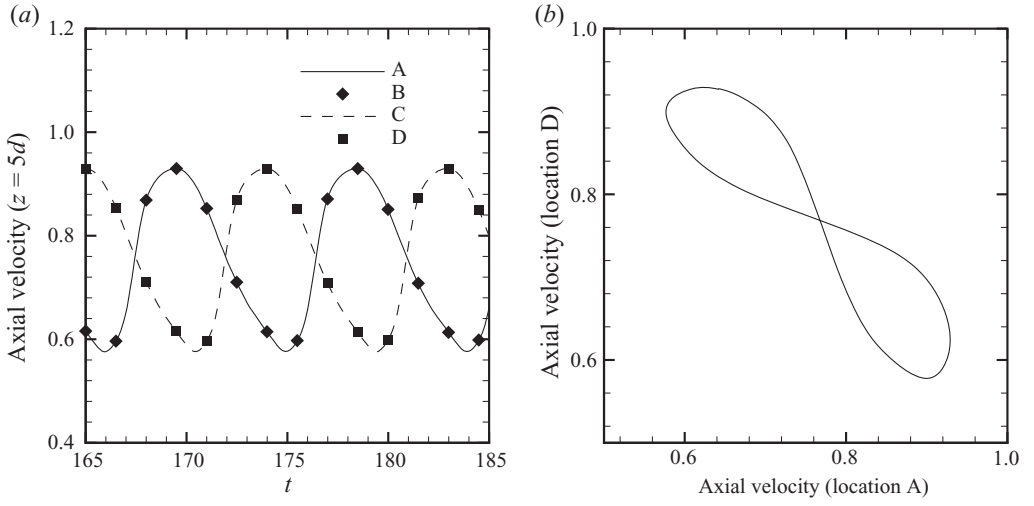

FIGURE 15. Influence of the 'double-sided' vortex shedding mode on the axial velocity variation in the wake at $z = 5d$ for $\chi = 4$ at $Re = 240$: (a) temporal variation of axial velocity at angular location of A, B, C and D (see figure 2b); (b) Lissajous pattern of axial velocity at locations A and D.

$St = 0.122$. A comparison of the axial velocities at locations A, B, C and D, shown in figure 15(a), indicates the presence of a symmetry plane as the velocity at location A matches that at B; similarly there is a correlation between axial velocity at locations C and D. Furthermore, a phase difference of 180° was observed between the velocity fluctuations at locations A and D. A Lissajous plot of the axial velocity fluctuation is shown in figure 15(b), where we observe that for $\chi = 4$ there is a double loop.

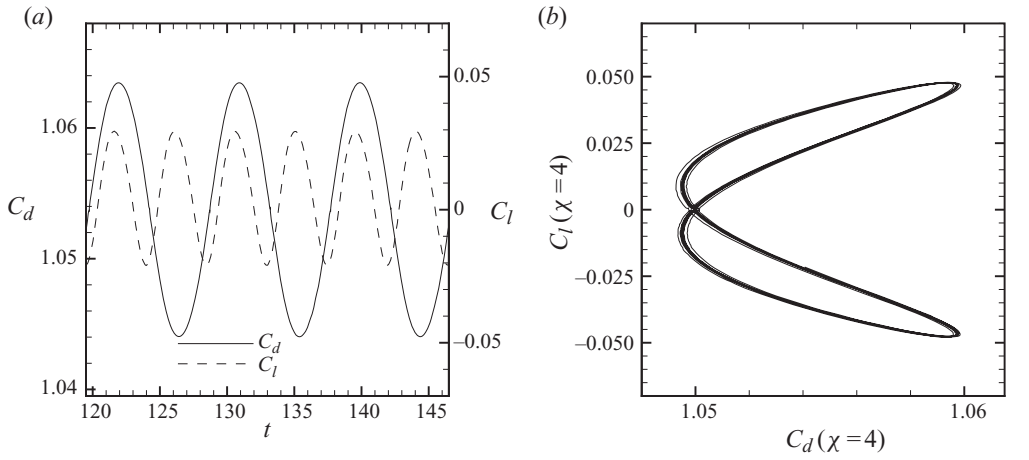

FIGURE 16. Influence of the 'double-sided' vortex shedding mode on the drag (C_d), and lift coefficient (C_l) for $\chi = 4$, at $Re = 240$: (a) temporal variation of C_d and C_l; (b) Lissajous plot of C_d and C_l.

In figure 16(a) periodic variations of the drag (C_d), and lift coefficient (C_l), which was computed using the lateral force acting along the symmetry plane, are shown. The lift coefficient was found to vary at the same frequency as the axial velocity fluctuation but the drag coefficient had fluctuations of twice the frequency. This difference, i.e. doubling in frequency, can be attributed to the 'double-sided' vortex shedding observed for $\chi = 4$. The 'double-sided' vortex shedding resulted in lift coefficient varying symmetrically in the positive and negative direction, a resultant of the spatio-temporal symmetry (see figure 16a). A Lissajous plot of C_d and C_l, shown in figure 16(b), indicates a double-looped structure similar to that observed for the velocity Lissajous plot (see figure 15b). The 'double-sided' vortex shedding leads to symmetric forces and torque to act on disk.

3.2. *Moving disk*

In this section, we describe the motion of a freely falling disks of $\chi = 2$ and 4 computed at $Re = 240$. The disk was released from rest and allowed to fall vertically against the action of gravity. After a period of steady fall, vortex shedding was observed behind the disk which eventually led to periodic lateral and angular oscillations.

3.2.1. *Motion of a disk of* $\chi = 2$

The three-dimensional trajectory of the disk of $\chi = 2$ is shown in figure 17(a), where it can be seen observed that the motion of the disk lies in a plane, where it should be noted that the z-axis is scaled differently compared to the xy-axes. The lateral oscillations of the disk are coupled with angular oscillations as shown in figure 17(b), where the motion of the disk is plotted in its plane of oscillation. The vortex structures shed from the disk using the λ_2-criterion is shown in figure 17(c) for a period of oscillation. For a more detailed visualization, animations of the vortex shedding process have been included in the on-line supplementary material (Movie 5). The movie shows the vortex regions determined with the λ_2-scheme, while the trajectory of the disk agrees with the experimental observations by Fernandes *et al.* (2007).

The disk oscillated at $St_b = 0.116$, which is comparable to the Strouhal number ($St = 0.122$) observed in the wake of the 'fixed' disk. In figure 18(a), the variation

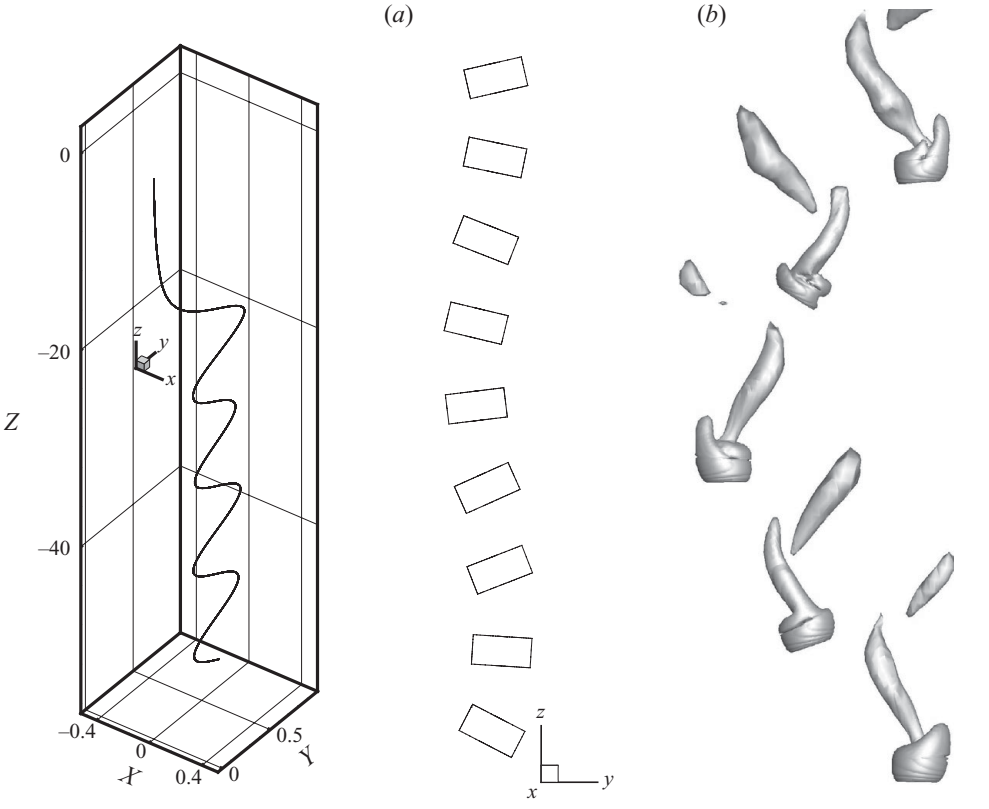

FIGURE 17. Trajectory of a freely falling disk of $\chi = 2$ at $Re = 240$: (*a*) three-dimensional trajectory of the disk; (*b*) motion of the disk in its oscillation plane; (*c*) vortex structures behind the disk visualized using the λ_2-criterion for single period of oscillation.

in lateral and angular displacements is plotted for different vertical locations for $\chi = 2$. The figure indicates a lateral displacement amplitude of approximately $0.232d$, which compares with the value of $0.22d$ obtained experimentally by Fernandes *et al.* (2007). The angular displacement has an amplitude of 26.82°, which is higher than the experimental value of 18° (Fernandes *et al.* 2007). From figure 18(*a*), comparing the lateral and angular displacements, we see that the disk has zero angular displacement, i.e. its axis is vertical at the extreme lateral positions. In figure 18(*b*) the linear and angular velocities are plotted for different vertical locations and $\chi = 2$. The lateral velocity in figure 18(*b*) has an amplitude of 0.093 and the angular velocity has an amplitude of 10.16 degree s^{-1}. The angular and lateral velocities have a phase difference of 83°, which compares with the experimental measurement of 97° (Fernandes *et al.* 2007). This implies that at the extremum of lateral displacement, where the lateral velocity is zero, the angular velocity is close an extremum.

3.2.2. *Motion of a disk of* $\chi = 4$

The motion of a freely falling disk of $\chi = 4$ was computed at $Re = 240$. The disk was released from rest and allowed to fall vertically against the action of gravity. After a period of steady fall, vortex shedding was observed behind the disk which eventually led to periodic lateral and angular oscillations. The three-dimensional trajectory of the disk is shown in figure 19(*a*), where it can be seen that the motion of the disk

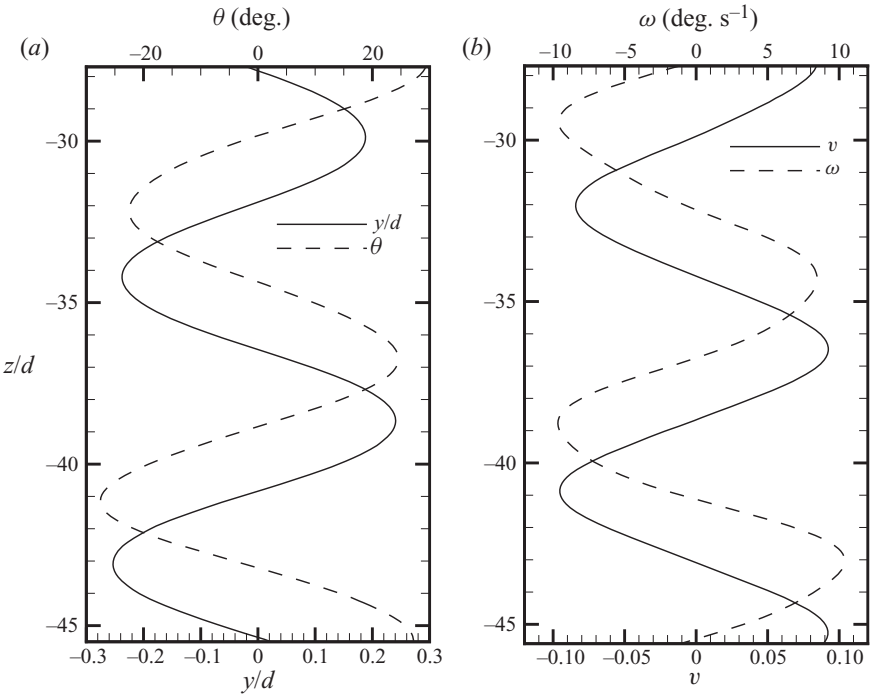

FIGURE 18. Planar oscillatory planar motion of a freely falling disk of $\chi = 2$ at $Re = 240$: (*a*) lateral and angular displacements as a function of the vertical displacement; (*b*) lateral and angular velocities as a function of the vertical coordinate.

lies in a plane. It should be noted that the z-axis is scaled differently compared to the xy-axes. The lateral oscillations of the disk are coupled with angular oscillations as shown in figure 19(*b*), where the motion of the disk is plotted in its plane of oscillation. The vortex structures shed from the disk using the λ_2-criterion is shown in figure 19(*c*) for a period of oscillation. For a more detailed visualization, animations of the vortex shedding process have been included in the on-line supplementary material (Movie 6). The movie visualizes the vortex regions determined with the λ_2-scheme. The trajectory of the disk agrees with the experimental observations by Fernandes *et al.* (2007).

The disk oscillated at $St_b = 0.171$, which is considerably higher than the Strouhal number ($St = 0.122$) observed in the wake of the fixed disk. In figure 20(*a*), the variation in lateral and angular displacements is plotted for different vertical locations. The figure indicates a lateral displacement amplitude of approximately $0.159d$. The angular displacement has an amplitude of 25.71°. From figure 20(*a*), comparing the lateral and angular displacements, it is apparent that the disk exhibits maximal angular displacements at the extreme lateral positions. In figure 20(*b*), the linear and angular velocities are plotted for different vertical locations. The lateral velocity in figure 20(*b*) has an amplitude of 0.0812 and the angular velocity has an amplitude of 10 degree s^{-1}. The angular and lateral velocities have a phase difference of 21° which differs from the experimental measurement of 51° (Fernandes *et al.* 2007). This discrepancy was previous noted in figure 6 and would require further improvement of the numerical model.

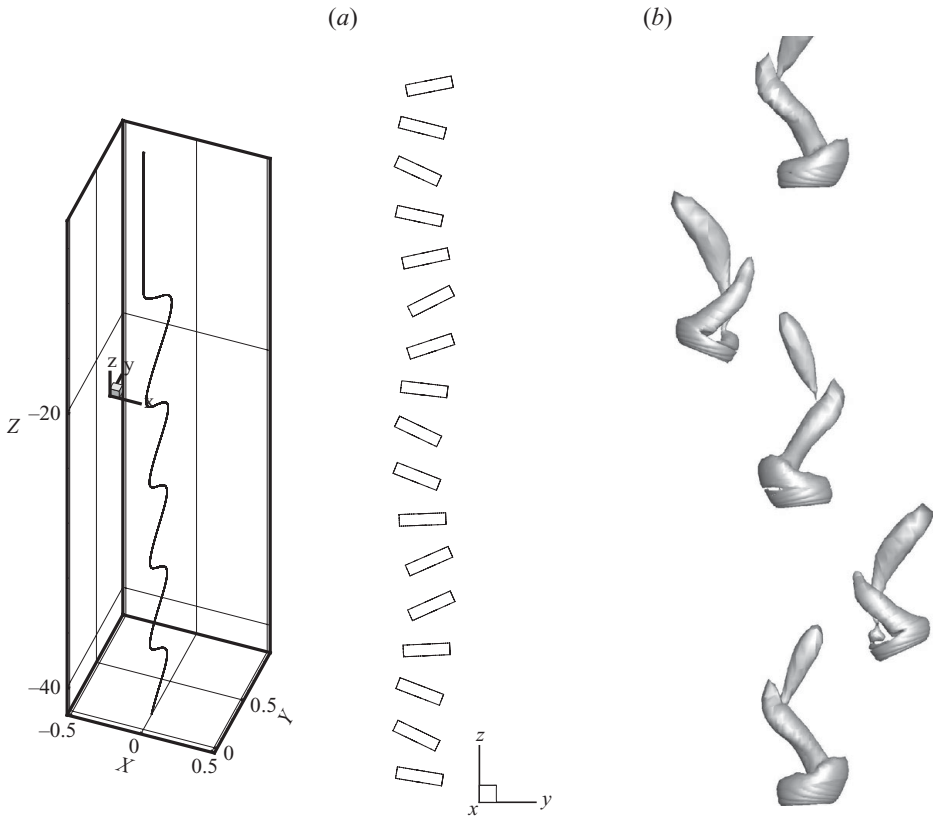

FIGURE 19. Trajectory of a freely falling disk of $\chi = 4$ at $Re = 240$: (*a*) three-dimensional trajectory of the disk; (*b*) motion of the disk in its oscillation plane; (*c*) vortex structures behind the disk visualized using the λ_2-criterion for single period of oscillation.

4. Conclusion

In this study, employing an experimentally validated computer simulation model, we first analysed the flow field around a fixed disk of $\chi = 2$ and 4 at a fixed Reynolds number of 240. The aspect ratio was found to significantly affect the vortex structures in the wake of the disk. Two different vortex shedding modes were identified as (see table 2):

(*a*) 'Single-sided' vortex shedding ($\chi = 2$): characterized by one-sided vortex loops (see figure 7) and asymmetric lateral forces (see figure 12*a*). A 'spatial' symmetry plane was observed in the flow field. The Strouhal number calculated using the axial velocity fluctuation was 0.122. This vortex shedding mode is similar to that observed in the wake of a fixed sphere at moderate Reynolds numbers (Johnson & Patel 1999).

(*b*) 'Double-sided' vortex shedding mode ($\chi = 4$): characterized by double-sided vortex loops which are shed alternately from diametrically opposite locations (see figure 8), resulting in symmetric positive and negative lateral forces (see figure 16*b*). A spatial symmetry plane (similar to that for $\chi = 2$) and a 'spatio-temporal' symmetry plane was observed in the flow field. The Strouhal number, calculated using the axial velocity fluctuation, was 0.122.

The motion of the disks of $\chi = 2$ and 4, falling freely due to the action of gravity at a fixed Reynolds number of 240 was computed. A comparison of their motion showed

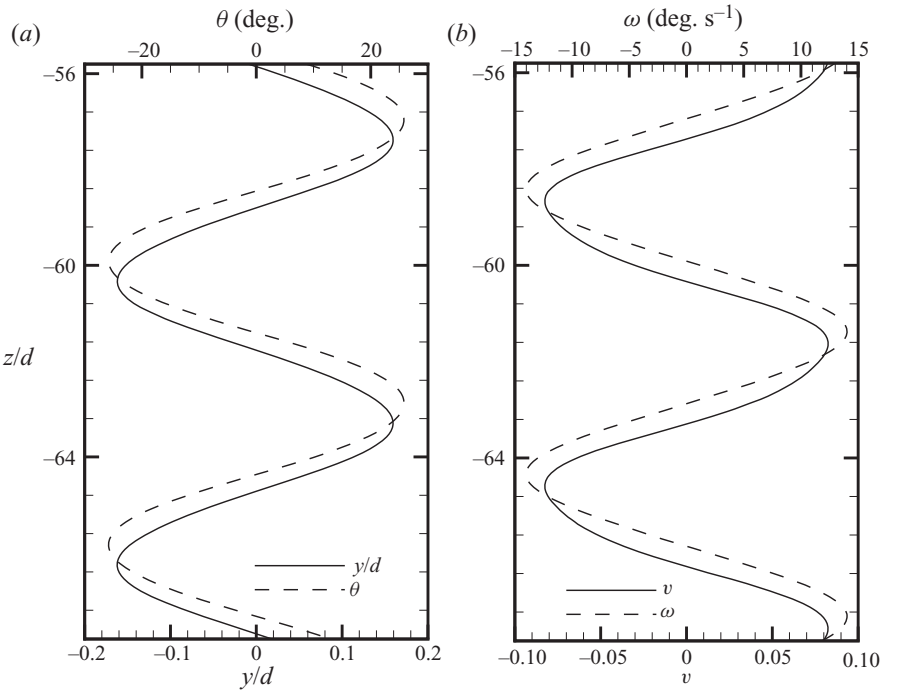

FIGURE 20. Oscillatory planar motion of a freely falling disk of $\chi = 4$ at $Re = 240$: (*a*) lateral and angular displacements as a function of the vertical displacement; (*b*) lateral and angular velocities as a function of the vertical coordinate.

considerable difference in the trajectories of the disks. The disk of $\chi = 2$ oscillated at nearly the same frequency as the vortex shedding observed behind a fixed disk of $\chi = 2$. The motion was characterized by the phase difference between the lateral and angular velocities, which was found to be a lag of 83°. The disk of $\chi = 4$ oscillated at a Strouhal number of 0.171, which is higher than the fluctuation frequency observed behind the fixed disk, namely $St = 0.122$. The phase difference between the lateral and angular velocities was found to be a lag of 21°. The phase difference between lateral and angular velocities, obtained from our numerical simulations, although match observed experimental trend (Fernandes *et al.* 2007), differ in magnitude. This deviation could mean an improvement in our numerical model for representing the fluid–structure interaction.

Future work on the influence of aspect ratio (non-sphericity) on the motion of axisymmetric objects such as disks, ellipsoids, etc. is planned. This study would help develop realistic models for computing trajectories of these particles in complex flow fields observed, for example, in the human respiratory tract.

The first author (A. R. Shenoy) would like to thank Roopa Jha for valuable suggestions during the course of this work. The second author (C. Kleinstreuer) gratefully acknowledges the support of AFOSR grant FA9550-05-1-0461 (Dr Walt Kozumbo, Program Manager) and NSF grant CBET-0834054 (Dr Marc S. Ingber, Program Director). The authors acknowledge the use of ICEM-CFD and ANSYS-CFX10 (Ansys Inc., Canonsburg, PA) as part of the Ansys-CM-P Lab academic

partnership. We would like to thank all the reviewers for their detailed and insightful feedback that has certainly played a major role in improving the quality of this paper.

Appendix A. Virtual mass coefficient

The virtual-mass tensors ($\boldsymbol{A}$) for translational motion of a disk (see (2.13)) has been computed by Loewenberg (1993) and curve-fitted by Fernandes *et al.* (2008) using the following expressions:

$$\boldsymbol{A}_{11} = \boldsymbol{A}_{22} = \frac{7d^3\rho_f}{12}\chi^{-3/4}, \tag{A 1}$$

$$\boldsymbol{A}_{33} = \frac{d^3\rho_f}{3}(\chi + 0.5\chi^{1/2}). \tag{A 2}$$

The added moment of inertia tensor ($\boldsymbol{D}$) for rotational motion of a disk (see (2.12)) has been estimated by Fernandes *et al.* (2008) by following an expression based on the known asymptotic value for a flat disk, i.e. when $\chi \to \infty$:

$$\boldsymbol{D}_{11} = \boldsymbol{D}_{22} = \frac{d^3\rho_f}{90}(\chi + 0.8\chi^{1/2}). \tag{A 3}$$

In the present study, we computed $\boldsymbol{A}$ and $\boldsymbol{D}$ by solving the Laplace equation for the potential function Φ for inviscid flow over a disk subject to an impulsive motion (Milne-Thomson 1996). The normal velocity boundary condition was applied to the disk surface ($\partial\sigma$) and the far field was assumed to be unaffected by the motion. The computational grid shown in figure 3 was used to solve for Φ. Specifically,

$$\boldsymbol{n}\cdot\nabla\Phi|_{\partial\sigma} = \boldsymbol{n}\cdot(\Delta\tilde{\boldsymbol{U}} + \boldsymbol{r}\times\Delta\tilde{\boldsymbol{\Omega}}), \quad \Phi(\boldsymbol{r}\to\infty) = 0, \tag{A 4}$$

where $\boldsymbol{n}$ is the unit normal to the disk surface, $\Delta\boldsymbol{U}$ and $\Delta\boldsymbol{\Omega}$ are the imposed changes in linear and angular velocities. To determine $\boldsymbol{A}$, we set $\Delta\boldsymbol{\Omega} = 0$, $\Delta\boldsymbol{U} = (1, 1, 1)$ and solved the Laplace equation to obtain Φ. The added-mass coefficient is then determined by integrating the force due to the impulse pressure, namely $\Pi = -\rho_f\Phi$ over the disk surface as shown below:

$$\boldsymbol{A}_{ii} = -\boldsymbol{e}_i\cdot\iint_{\partial\sigma}\Pi\,\mathrm{d}\boldsymbol{S}, \tag{A 5}$$

where $\boldsymbol{e}_i$ is a unit vector along the i^{th} direction. Similarly, to determine $\boldsymbol{D}_{11}$ we set $\Delta\boldsymbol{U} = 0$ and $\Delta\boldsymbol{\Omega} = (1, 0, 0)$ and solved the Laplace equation to obtain Φ. The added-moment of inertia coefficient is then determined by integrating the torque due to the impulse pressure as shown below:

$$\boldsymbol{D}_{ii} = -\boldsymbol{e}_i\cdot\iint_{\partial\sigma}\Pi\,\boldsymbol{r}\times\mathrm{d}\boldsymbol{S}, \tag{A 6}$$

The results obtained from these computations were compared with those of Fernandes *et al.* (2008) (see figure 21). A good comparison was observed for $\boldsymbol{A}$ but, slight discrepancies are noticed for $\boldsymbol{D}$, which was obtained by matching only the asymptotic value at $\chi \to \infty$. Hence, we propose the following modified formula for the added-moment coefficient that matches our numerical results:

$$\boldsymbol{D}_{11} = \boldsymbol{D}_{22} = \frac{d^3\rho_f}{90}(\chi + 0.2\chi^{1/2}). \tag{A 7}$$

The added-moment coefficient $\boldsymbol{D}_{33}$ is zero due to symmetry.

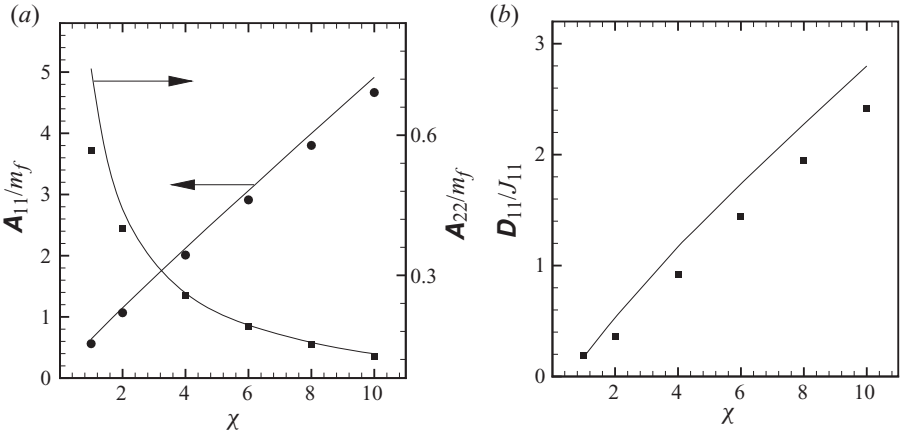

FIGURE 21. A comparison of the computed virtual-mass coefficients, against theoretical results obtained from Fernandes *et al.* (2008), as a function of aspect ratio: (*a*) components of the added-mass tensor (***A***) non-dimensionalized using the mass of the displaced fluid (m_f); (*b*) component of the added-moment of inertia tensor (***D***) non-dimensionalized using the rotational moment of inertial J_{11}.

Appendix B. Euler angle calculations

The Euler parameters $\Theta = (\varepsilon_1, \varepsilon_2, \varepsilon_3, \eta)^T$ can be computed from the Euler angles (ϕ, θ, ψ) using the relationships given below (Goldstein *et al.* 2002):

$$\varepsilon_1 = \cos\frac{\phi-\psi}{2}\sin\frac{\theta}{2}, \quad \varepsilon_2 = \sin\frac{\phi-\psi}{2}\sin\frac{\theta}{2}, \tag{B 1}$$

$$\varepsilon_3 = \sin\frac{\phi+\psi}{2}\cos\frac{\theta}{2}, \quad \eta = \cos\frac{\phi+\psi}{2}\cos\frac{\theta}{2}. \tag{B 2}$$

The initial orientation of the disk was specified in terms of the Euler angles, which was then used to compute the Euler parameters. The equations of rotational motion were then computed using the Euler parameters. The rotational transformation matrix ***R*** and the matrix describing the rate of change of the Euler parameters ***E*** were computed using the following relationships (Goldstein *et al.* 2002):

$$\boldsymbol{R} = \begin{pmatrix} 1-2(\varepsilon_2^2+\varepsilon_3^2) & 2(\varepsilon_1\varepsilon_2+\varepsilon_3\eta) & 2(\varepsilon_1\varepsilon_3-\varepsilon_2\eta) \\ 2(\varepsilon_2\varepsilon_1-\varepsilon_3\eta) & 1-2(\varepsilon_3^2+\varepsilon_1^2) & 2(\varepsilon_2\varepsilon_3+\varepsilon_1\eta) \\ 2(\varepsilon_3\varepsilon_1+\varepsilon_2\eta) & 2(\varepsilon_3\varepsilon_2-\varepsilon_1\eta) & 1-2(\varepsilon_1^2+\varepsilon_2^2) \end{pmatrix}, \tag{B 3}$$

$$\boldsymbol{E} = \begin{pmatrix} \eta & -\varepsilon_3 & \varepsilon_2 \\ \varepsilon_3 & \eta & -\varepsilon_1 \\ -\varepsilon_2 & \varepsilon_1 & \eta \\ -\varepsilon_1 & -\varepsilon_2 & -\varepsilon_3 \end{pmatrix}. \tag{B 4}$$

All computations for the body motion were performed using the Euler parameters. The Euler angles were then back calculated from the Euler parameters for output.

Supplementary movies are available at journals.cambridge.org/flm.

REFERENCES

Abelev, A. V., Valent, P. J. & Holland, K. T. 2007 Behaviour of a large cylinder in free-fall through water. *IEEE J. Ocean. Engng* **32** (1), 10–20.

Achenbach, E. 1974 Vortex shedding from spheres. *J. Fluid Mech.* **62**, 209–221.

Auguste, F., Fabre, D. & Magnaudet, J. 2010 Bifurcations in the wake of a thick circular disk. *Theor. Comput. Fluid Dyn.* **24**, 305–313.

Barkley, D. & Henderson, R. D. 1996 Three-dimensional Floquet stability analysis of the wake of a circular cylinder. *J. Fluid Mech.* **322**, 215–241.

Barth, T. & Jespersen, D. 1989 The design and application of upwind schemes on unstructured meshes. AIAA *Paper* 89–0366.

Belmonte, A., Eisenberg, H. & Moses, E. 1998 From flutter to tumble: inertial drag and Froude similarity in falling paper. *Phys. Rev. Lett.* **81** (2), 345–348.

Berger, E., Scholz, D. & Schumm, M. M. 1990 Coherent vortex structures in the wake of a sphere and a circular disk at rest and under forced vibrations. *J. Fluids Struct.* **4**, 231–257.

Brücker, C. 2001 Spatio-temporal reconstruction of vortex dynamics in axisymmetric wakes. *J. Fluids Struct.* **15** (3–4), 543–554.

Crowder, T. M., Rosati, J. A., Schroeter, J. D., Hickey, A. J. & Martonen, T. B. 2002 Fundamental effects of particle morphology on lung delivery: predictions of Stokes law and the particular relevance to dry powder inhaler formulation and development. *Pharm. Res.* **19** (3), 239–245.

Demirdžić, I. & Peric, M. 1988 Space conservation law in finite volume calculations of fluid flow. *Intl J. Numer. Methods Fluids* **8** (9), 1037–1050.

Demirdžić, I. & Peric, M. 1990 Finite volume method for prediction of fluid flow in arbitrarily shaped domains with moving boundaries. *Intl J. Numer. Methods Fluids* **10** (7), 771–790.

Fernandes, P. C., Ern, P., Risso, F. & Magnaudet, J. 2005 On the zigzag dynamics of freely moving axisymmetric bodies. *Phys. Fluids* **17** (9), 098107.

Fernandes, P. C., Ern, P., Risso, F. & Magnaudet, J. 2008 Dynamics of axisymmetric bodies rising along a zigzag path. *J. Fluid Mech.* **606**, 209–223.

Fernandes, P. C., Risso, F. R., Ern, P. & Magnaudet, J. 2007 Oscillatory motion and wake instability of freely rising axisymmetric bodies. *J. Fluid Mech.* **573**, 479–502.

Field, S. B., Klaus, M., Moore, M. G. & Nori, F. 1997 Chaotic dynamics of falling disks. *Nature* **388**, 252–254.

Goldstein, H., Poole, C. & Safko, J. 2002 *Classical Mechanics*. Addison Wesley.

Haller, G. 2005 An objective definition of a vortex. *J. Fluid Mech.* **525**, 1–26.

Jenny, M., Dušek, J. & Bouchet, G. 2004 Instabilities and transition of a sphere falling or ascending freely in a newtonian fluid. *J. Fluid Mech.* **508**, 201–239.

Jeong, J. & Hussain, F. M. 1995 On the identification of a vortex. *J. Fluid Mech.* **285**, 69–94.

Johnson, T. A. & Patel, V. C. 1999 Flow past a sphere up to a Reynolds number of 300. *J. Fluid Mech.* **378**, 19–70.

Kleinstreuer, C. 2006 *Biofluid Dynamics: Principles and Selected Applications*. CRC Press, Taylor & Francis Group.

Kleinstreuer, C., Zhang, Z. & Donohue, J. F. 2008 Targeted drug-aerosol delivery in the human respiratory system. *Annu. Rev. Biomed. Engng* **10** (1), 195–220.

Loewenberg, M. 1993 Stokes resistance, added mass, and basset force for arbitrarily oriented, finite-length cylinders. *Phys. Fluids* **5** (3), 765–767.

Magarvey, R. H. & Maclatchy, C. S. 1965 Vortices in sphere wakes. *Can. J. Phys.* **43**, 1649–1656.

Marchildon, E. K., Clamen, A. & Gauvin, W. H. 1964 Drag and oscillatory motion of freely falling cylindrical particles. *Can. J. Chem. Engng* **42**, 178–182.

Milne-Thomson, L. M. 1996 *Theoretical Hydrodynamics*. Dover.

Mordant, N. & Pinton, J. F. 2000 Velocity measurement of a settling sphere. *Eur. Phys. J.* B **18** (2), 343–352.

Mougin, G. & Magnaudet, J. 2002 The generalized Kirchhoff equations and their application to the interaction between a rigid body and an arbitrary time-dependent viscous flow. *Intl J. Multiph. Flow* **28** (11), 1837–1851.

Perry, A. E., Lim, T. T. & Chong, M. S. 1980 The instantaneous velocity fields of coherent structures in coflowing jets and wakes. *J. Fluid Mech.* **101** (02), 243–256.

Press, W. H., Teukolsky, S. A., Vetterling, W. T. & Flannery, B. P. 1992 *Numerical Recipes in FORTRAN: The Art of Scientific Computing*. Cambridge University Press.

Rhie, C. M. & Chow, W. L. 1983 Numerical study of the turbulent flow past an airfoil with trailing edge separation. *AIAA J.* **21** (11), 1525–1532.

Ross, F. W. & Willmarth, W. W. 1971 Some experimental results on sphere and disk drag. *AIAA J.* **9**, 285–291.

Shenoy, A. R. & Kleinstreuer, C. 2008 Flow over a thin circular disk at low-to-moderate Reynolds numbers. *J. Fluid Mech.* **605**, 253–262.

Skotheim, J. M. & Secomb, T. W. 2007 Red blood cells and other nonspherical capsules in shear flow: oscillatory dynamics and the tank-treading-to-tumbling transition. *Phys. Rev. Lett.* **98** (7), 078301.

Stewart, R. E. & List, R. 1983 Gyrational motion of disks during free-fall. *Phys. Fluids* **26** (4), 920–927.

Van Doormaal, J. P. & Raithby, G. D. 1984 Enhancements of the SIMPLE method for predicting incompressible flows. *Numer. Heat Transfer* A **7** (2), 147–163.

Wang, Z., Hopke, P. K., Ahmadi, G., Cheng, Y. & Baron, P. A. 2008 Fibrous particle deposition in human nasal passage: the influence of particle length, flow rate, and geometry of nasal airway. *J. Aerosol Sci.* **39** (12), 1040–1054.

Willmarth, W. W., Hawk, N. E. & Harvey, R. L. 1964 Steady and unsteady motions and wakes of freely falling disks. *Phys. Fluids* **7**, 197–208.

Yin, C., Rosendahl, L., Kær, S. K. & Condra, T. J. 2004 Use of numerical modelling in design for co-firing biomass in wall-fired burners. *Chem. Engng Sci.* **59** (16), 3281–3292.